# Faceting transition in aluminum as a grain boundary phase transition

Yoonji Choi (최윤지) and Tobias Brink*
*Max Planck Institute for Sustainable Materials, Max-Planck-Straße 1, 40237 Düsseldorf, Germany*
(Dated: 4 August 2025)

Grain boundaries facet due to anisotropic grain boundary energies: While the faceted boundary has a larger area than the corresponding straight boundary, a significantly lower energy of the facets compared to a straight segment can drive the faceting. This picture is complicated by faceting/defaceting transitions where the free energy difference between the two states depends on the temperature. Such transitions have been observed and modeled before, but their exact nature was not fully understood. Here, we use atomistic computer simulations to show that a well known faceting transition in $\Sigma3$ $[11\bar{1}]$ tilt grain boundaries in Al is in fact a grain boundary phase transition (also called complexion transition). This means that the faceted and defaceted boundaries are associated with different atomic structures, which have different thermodynamic stability ranges. At low temperatures, the grain boundary phase associated with faceting is stable, while at high temperatures the flat grain boundary phase is stable. We also report on our thorough tests of Al interatomic potentials for this purpose, which include comparisons to density-functional theory calculations. Our chosen potential performs well for our grain boundaries. As a consequence we were able to obtain results that align with previous experimental results.

## I. INTRODUCTION

Grain boundaries (GBs) are abundant planar defects in polycrystalline materials. While these defects are not thermodynamically stable, the transformation from polycrystals to single crystals is often so slow at the application temperature that the defective system is in a deep local free energy minimum [1, 2]. In well-relaxed systems, GBs therefore still transform into energetically favorable states [3]. If the excess free energy of a GB is highly anisotropic with regards to the crystallographic plane it occupies, GB faceting can occur [4–10]. There, the GB increases its GB area by splitting into facets on low-energy planes, thereby decreasing its overall free energy despite its higher GB area. Typically, the facets have a driving force to grow in size, because the line defects separating the facets (facet junctions) are also connected to an energy cost [8, 9, 11–15].

Reversible faceting/defaceting transitions—wherein the GB switches between a faceted and a flat state with changing temperature—have been observed. The most famous example is the $\Sigma3$ $[11\bar{1}]$ (011) tilt GB in Al, which splits into {112} facets at low temperatures [6, 9, 16]. The explanation for this reversible defect transition must lie in the relative free energies of the faceted and flat GBs. The free energy of a GB is, however, not just a function of the macroscopic GB parameters (misorientation between the crystallites and GB plane), but also of the GB structure. In analogy to bulk phases, we can treat these different structures of the interface as GB phases [17], also called complexions [18–21]. These are distinct from bulk phases that nucleate at the GB, such as precipitates or wetting phases [21, 22], but are instead constrained to the interface and can be described by interface thermodynamics [17, 20–29]. We can categorize GB phase transitions into congruent transitions, where the macroscopic GB parameters remain the same while the atomic structure of the GB changes; and non-congruent transitions, where also the macroscopic GB parameters change. Faceting/defaceting transitions would thus be non-congruent GB phase transitions.

In $[11\bar{1}]$ tilt GBs of fcc metals with misorientation $\theta < 60°$ (the $\Sigma3$ boundary has a misorientation of exactly 60°), several GB phases were found [Fig. 1(d)] [30–35]. On the near-(011) plane, congruent transitions between the "domino" and "pearl" phases were found in Cu [30, 32] and predicted by simulations for many fcc metals [34]. On the near-(112) planes, only a "zipper" phase was found [31, 33]. Recently, the domino phase was identified as consisting of nanoscale zipper facets, which is only possible for $\theta < 60°$ [15]. For $\theta = 60°$, these facets become macrofacets. Thus, if a congruent domino-to-pearl GB phase transition exists, this raises the question if the faceting/defaceting transition in $\Sigma3$ $[11\bar{1}]$ (011) GBs is a non-congruent version of this transition. If a pearl-like phase exists, it might be more stable at high temperatures than a faceted zipper GB. Here, we explore this hypothesis with atomistic simulatons.

## II. THEORY

### A. Grain boundary phases and their bicrystallography

In order to better understand the GB phases involved, we will quickly discuss the crystallography and atomic structures of the relevant GBs. There are two sets of high-symmetry GB planes in $\Sigma3$ $[11\bar{1}]$ tilt GBs ($\theta = 60°$), as indicated in the dichromatic pattern in Fig. 1(a). These planes are inclined by 30° towards each other. The structure of the {112} GB planes has been identified before as the zipper GB phase [Fig. 1(b)] in Al at room temperature

* t.brink@mpie.de

Published in:
Choi and Brink, Phys. Rev. Mater. **9**, 083607 (2025) DOI: 10.1103/2dnf-zdz8

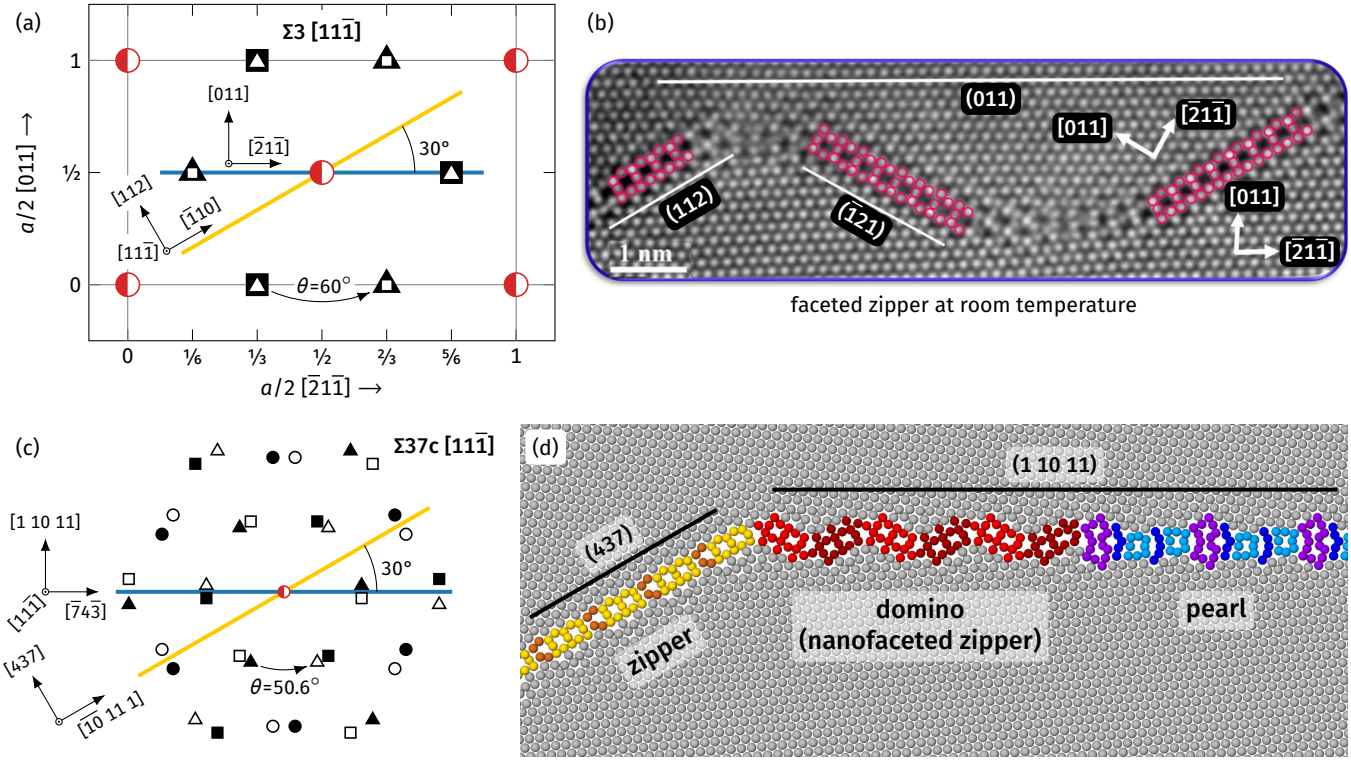


FIG. 1. (a) Dichromatic pattern of Σ3 [11$\bar{1}$] tilt GBs. Black and white symbols represent the atoms of the two crystallites, while the shape of the symbols represents the different (11$\bar{1}$) planes on which these atoms lie. The black and white symbols coincide in the projection, but are located on different planes. The red data points are coincidence sites. The crystal directions refer to the coordinate system of the lower crystallite. Two possible (quasi-)symmetric GB planes are indicated. (b) At room temperature, faceted zipper structures were observed experimentally in Al on {112} planes. The structure on the (011) plane is not reported in the literature. Image from Ref. [35] with crystallographic directions and planes adjusted to the convention of the present paper. Reused under the terms of the Creative Commons Attribution 4.0 International license (https://creativecommons.org/licenses/by/4.0/). (c) Excerpt of the dichromatic pattern of a Σ37c [11$\bar{1}$] tilt GB. The red data point is a coincidence site. The full dichromatic pattern can for example be found in the supplemental material of Ref. [32]. (b) Snapshot of a simulation of the corresponding GB phases. The domino phase consists of nanoscale facets of zipper structures [15]. This nanofaceting is impossible in the Σ3 GB, where the facets are energetically driven to grow [15]. We hypothesize that pearl-like phases may exist on the (011) plane of Σ3.

[35, 36]. This GB has a mirror symmetry across its GB plane and is therefore a symmetric GB. The Σ3 [11$\bar{1}$] {011} GBs have crystallographically equivalent planes on both sides of the GB, but the GB plane is not a mirror plane. Those GBs are called quasi-symmetric in the nomenclature of Morawiec [37]. At room temperature, faceting into {112} zipper facets was observed in Al [35], but if a non-faceted GB phase existed on the {011} planes, it could be responsible for a non-congruent faceting/defaceting transition.

A related transition does indeed exist for $\theta < 60°$. Figure 1(c)–(d) shows the Σ37c [11$\bar{1}$] tilt GB as an example. We similarly obtain a set of symmetric {347} GB planes and quasi-symmetric {1 10 11} GB planes, inclined by 30° towards each other. While the Σ37c [11$\bar{1}$] {347} GBs also exhibit zipper GB phases, the {1 10 11} planes are home to the domino and pearl phases. A congruent domino-to-pearl transition exists [30, 32, 34], but a non-congruent faceting transition does not: any {1 10 11} plane with faceted zipper structures exhibits an unusual attractive interaction between the facet junctions and leads to nanofaceting [15]. This nanofaceted phase is the domino phase, as can also be confirmed by visual inspection of the motifs in Fig. 1(d). In the present work we look for a pearl-like phase in Σ3 GBs. Since nanofaceting is not possible for Σ3 boundaries [15], the congruent domino-to-pearl transition would become a non-congruent transition from zipper facets to a flat pearl-like phase.

### B. Grain boundary thermodynamics

GB phases can be described with few modifications from standard thermodynamics [17, 23–29]. Most importantly, GBs do not exist in thermodynamic equilibrium and we will thus have to work with metastable states in which the existence of a GB is postulated. As a further simplification for the purpose of this paper, we assume

that the bulk regions do not undergo phase transitions, but only the GB does. Additionally, we only consider pure, single-component materials. The Gibbs free energy $G$ of a bicrystal can be separated into [17]

$$G = G_1 + G_2 + \gamma A + G_{\text{surface}}, \tag{1}$$

where $G_1$ and $G_2$ are the free energies of the two crystallites, $G_{\text{surface}}$ accounts for the surface, $\gamma$ is the GB free energy and $A$ is the GB area. Ignoring surface and bulk phase transitions, we can describe GB phase transitions fully via excess properties. We assume $G_1/N_1 = G_2/N_2 = G_{\text{bulk}}/N_{\text{bulk}}$, where $N$ is the number of atoms and $G_{\text{bulk}}$ is the Gibbs free energy of a defect-free bulk region. Thus, we define the excess of any extensive property $Z$ as [29, 38]

$$[Z] = \frac{Z_{\text{GB}} - \frac{N_{\text{GB}}}{N_{\text{bulk}}} Z_{\text{bulk}}}{A}, \tag{2}$$

where $Z_{\text{GB}}$ is the value of $Z$ in a region containing a GB of area $A$ with $N_{\text{GB}}$ atoms.

Important excess properties in the present paper are thus [29, 38]

$$\gamma = [G] = [U] - T[S] - \sigma_{33}[V], \tag{3}$$

with internal energy $U$, entropy $S$, stress tensor $\sigma_{ij}$, and volume $V$. Here, we use the boundary conditions from Ref. [29], where the $z$ direction (index 3, normal to the GB plane) is under isobaric conditions with applied stress $\sigma_{33}$. The $x$ and $y$ directions are fixed so that the bulk lattice is unstrained at the given temperature $T$. In the present case, we are not interested in systems under stress (except for $\sigma_{33}$ in Appendix A), so we use shear stresses $\sigma_{31} = \sigma_{32} = 0$ and shear strain $\varepsilon_{12} = 0$. The treatment of nonzero shear is described elsewhere [29].

We assume ambient pressure for the faceting/defacting transition and thus simplify most of our investigation to $\sigma_{3i} \approx 0$:

$$\gamma = [U] - T[S]. \tag{4}$$

For statics simulations, we also define the useful property

$$\gamma_0 = [E_{\text{pot}}] \tag{5}$$

at $T = 0$, where $E_{\text{pot}}$ is the potential energy of the system with all atoms in minimum-energy positions. In general, quantum-mechanical zero-point vibrations mean that $\gamma_0 \neq \gamma(T{=}0)$. In MD simulations, classical systems are considered and $\gamma_0 = \gamma_{\text{MD}}(T{=}0)$.

Due to our definition (Eq. 2) of the excess, $[N] = 0$ even if atoms are added or removed in the GB region. Nevertheless, the difference of atoms per crystallographic plane between bulk and GB is physically meaningful [39, 40]. Since individual crystallographic planes may not be identifiable in the GB, the GB's planar fraction can be defined as [39]

$$\hat{n} = \frac{N_{\text{GB}}}{N_{\text{plane}}} \mod 1, \tag{6}$$

where $N_{\text{plane}}$ is the number of atoms in a defect-free crystallographic plane with the same area $A$ as the GB. It is necessary to vary $\hat{n}$ to find all GB phases [39]. The value of $\hat{n}$ does not affect the thermodynamics, but the transition between GB phases with different $\hat{n}$ requires diffusion and is thus typically much slower [39].

To aid in classification of the GB phases we also used the GB excess stresses, which are defined at $\sigma_{3i} = 0$ as

$$\hat{\tau}_{ij} = \frac{\hat{\sigma}_{ij} V_{\text{GB}}}{A} \qquad \text{for } i, j \in \{1, 2\}, \tag{7}$$

where $\hat{\sigma}_{ij}$ is the residual stress in a region of volume $V_{\text{GB}}$ that contains a GB with area $A$ [29]. These stresses are the result of the mismatch between bulk and GB while fixing the strains $\varepsilon_{11}$, $\varepsilon_{22}$, and $\varepsilon_{12}$.

## III. METHODS

Most calculations were performed with an empirical interatomic potential, namely the embedded atom method (EAM) potential by Zhakhovskii et al. [41] as downloaded from the NIST Interatomic Potentials Repository [42] (designated as "Zha09" in this paper). Other potentials were also tested as described in Appendix A. We used LAMMPS [43, 44] to perform molecular dynamics (MD) and statics simulations. In order to evaluate the potentials, we conducted additional density-functional theory (DFT) simulations using VASP 5.4.4 [45–48]. The simulations were set up, managed, and analyzed with PYIRON [49].

### A. Grain boundary structure search

The possible GB phases and their structures in $\Sigma 3$ $[11\bar{1}]$ tilt GBs with (quasi-)symmetric GB planes (011) and (112) were explored with the GRIP software [50]. This code automatically constructs GB supercells of varying size (here we used variations from $1 \times 1$ to $5 \times 5$ in the GB plane), applies a random displacement to one of the crystallites, removes a random fraction of atoms from the GB region, runs a canonical MD simulation with random temperature and duration with 95% probability, and then minimizes the atomic position with regards to the potential energy. This is repeated many times to collect various GB structures. High-energy structures are discarded regularly. For the (011) GB plane, we also ran a structure search with supercell sizes ranging from $1 \times 5$ to $1 \times 25$ (i.e., no repetition along the tilt axis and 5 to 25 repetitions along $y$ in the GB plane) to find additional faceted GBs with longer facet lengths.

All simulations cells were periodic in the $x$ direction, which lies along the tilt axis, and the $y$ direction, which also lies in the GB plane. We used open surfaces in the $z$ direction normal to the GB.

### B. Temperature-dependent free energy calculation and molecular dynamics simulation of grain boundary phase transitions

In single-element systems, the entropy is solely a vibrational entropy. We therefore computed the GB excess free energy $\gamma$ as a function of temperature $T$ for several GB phases of interest using the quasi-harmonic approximation (QHA) [51, 52]. Here, force constant matrices were obtained with the `dynamical_matrix` command in LAMMPS. Then the Helmholtz free energies were calculated as

$$F_{\text{classical}} = E_{\text{pot}} + k_B T \sum_{i=1}^{3N-3} \ln \frac{h\nu_i}{k_B T} \tag{8}$$

$$F_{\text{qm}} = E_{\text{pot}} + k_B T \sum_{i=1}^{3N-3} \ln \left[ 2 \sinh \left( \frac{\frac{1}{2} h\nu_i}{k_B T} \right) \right], \tag{9}$$

where the sum is over the phonon eigenfrequencies $\nu_i$ (excluding the three null values) obtained from the force constant matrix. We calculated free energies under the assumption of classical oscillators ($F_{\text{classical}}$), correspoding to classical MD simulations, and for quantum-mechanical oscillators ($F_{\text{qm}}$). These free energies were obtained at different cell volumes corresponding to different lattice constants. For each temperature, the relevant lattice constant was chosen in one of two ways. For the classical mechanics case, the lattice constant was obtained with an MD simulation. For the quantum mechanics case, we used the minimum free energy of the fcc structure as a function of volume at each temperature. The latter approach can be unreliable for certain potentials (see Appendix A), which is why we generally preferred the classical approach here. Finally, using a defect-free reference, we obtain the GB free energy as $\gamma(T) = [F(T)]$ as in Eq. 4.

In addition to the predictions by free-energy calculations, we also performed MD simulations on various GBs. We used a time integration step of 2 fs, Nosé–Hoover thermostats for the desired temperature, and a barostat at zero pressure for the periodic directions. These simulations were run for 30 ns to observe the resulting GB phase (faceted or straight). Visualization and structure analysis using the polyhedral template matching (PTM) method [53] were performed with OVITO [54].

### C. Density-functional theory

Due to the wide variety of available interatomic potentials for Al, we had to decide on the most well-suited one for our GB calculations. We therefore also calculated GB energy and excess volumes using density-functional theory (DFT) on the GB structures with (011) planes obtained with our structure search. To avoid vacuum in the DFT cell, we produced fully periodic cells with two equivalent GBs. We tested different amounts of bulk material between the GBs, up to cell sizes of roughly 100 atoms. GB excess properties were converged at that point (see Figs. S7–S9 in the Supplemental Material [55]). The results for the (112) plane (zipper structure) were taken from Refs. [36, 56].

We used the projector-augmented wave (PAW) method [57] within the generalized gradient approximation (GGA) with the Perdew–Burke–Ernzerhof (PBE) parametrization [58]. We employed PAW potentials [59] with three valence electrons ($3s^2\ 3p^1$). Following earlier work of one of us [36], high-accuracy parameters were used to ensure correct GB excess properties, which are very sensitive to numerical errors. Based on this, we used the previously obtained lattice constant of 4.040(5) Å for Al and performed simulations on the GBs with a plane-wave energy cutoff of 450 eV and a $27 \times 27 \times 2$ $k$-point mesh on a Γ-centered Monkhorst–Pack grid [60]. During structure minimization, forces were converged to 0.01 eV/Å.

The cell sizes in $x$ and $y$ direction (GB plane) were fixed in accordance with the fcc lattice constant to $7.00 \times 4.95$ Å$^2$ ($1 \times 1$ supercell). We varied the length of the cell in $z$ (normal to the GB) and fitted a third-order polynomial to the energy–length curve. This allowed us to obtain the energies and volumes as a function of $\sigma_{33}$, which is the derivative of this curve normalized by the GB area. By comparing a cell containing a GB with a similarly-sized defect-free cell, we obtained the excess properites $[U]$ and $[V]$ as functions of $\sigma_{33}$.

## IV. GRAIN BOUNDARY PHASES OF Σ3 [111] TILT BOUNDARIES

As a first step towards understanding the faceting transition in Σ3 $[11\bar{1}]$ tilt boundaries, we performed an extensive GB structure search with GRIP [50]. We performed this search for both of the possible (quasi-)symmetric GB plane types, here we used the (011) and (112) planes [Fig. 1(a)]. The GB structure discovery yielded thousands of structures with various GB energies, most of which are defective local minima or high-energy structures. We excluded GBs with $\gamma_0 > 0.49\,\text{J/m}^2$ for (011) and $\gamma_0 > 0.44\,\text{J/m}^2$ for (112) from further analysis, since they are too energetically unfavorable to occur in reality or in MD simulations.

To categorize the remaining structures, we evaluated their excess properties, the most important of which are plotted in Fig. 2. A principal component analysis (PCA) [61–63] performed on the excess properties $\gamma_0$, $[V]$, $\hat{\tau}_{11}$, and $\hat{\tau}_{22}$, reveals that the (011) GBs can be separated into at least 2 clusters, while the (112) GBs all belong to one cluster (see Supplemental Figs. S1 and S2 for more details on this analysis). By examination of the structures of low-energy GBs with (011) GB planes in each cluster, we identified two "B" structures (with $\hat{n} = 1/3$ and $2/3$), "square" structures, and faceted structures. The B ⅓ and square structures are structural units that also occur in the pearl phase in Σ37c $[11\bar{1}]$ (1 10 11) GBs shown in Fig. 1(d) [32]. The square motif also occurs in pearl GBs with lower misorientation angles than the

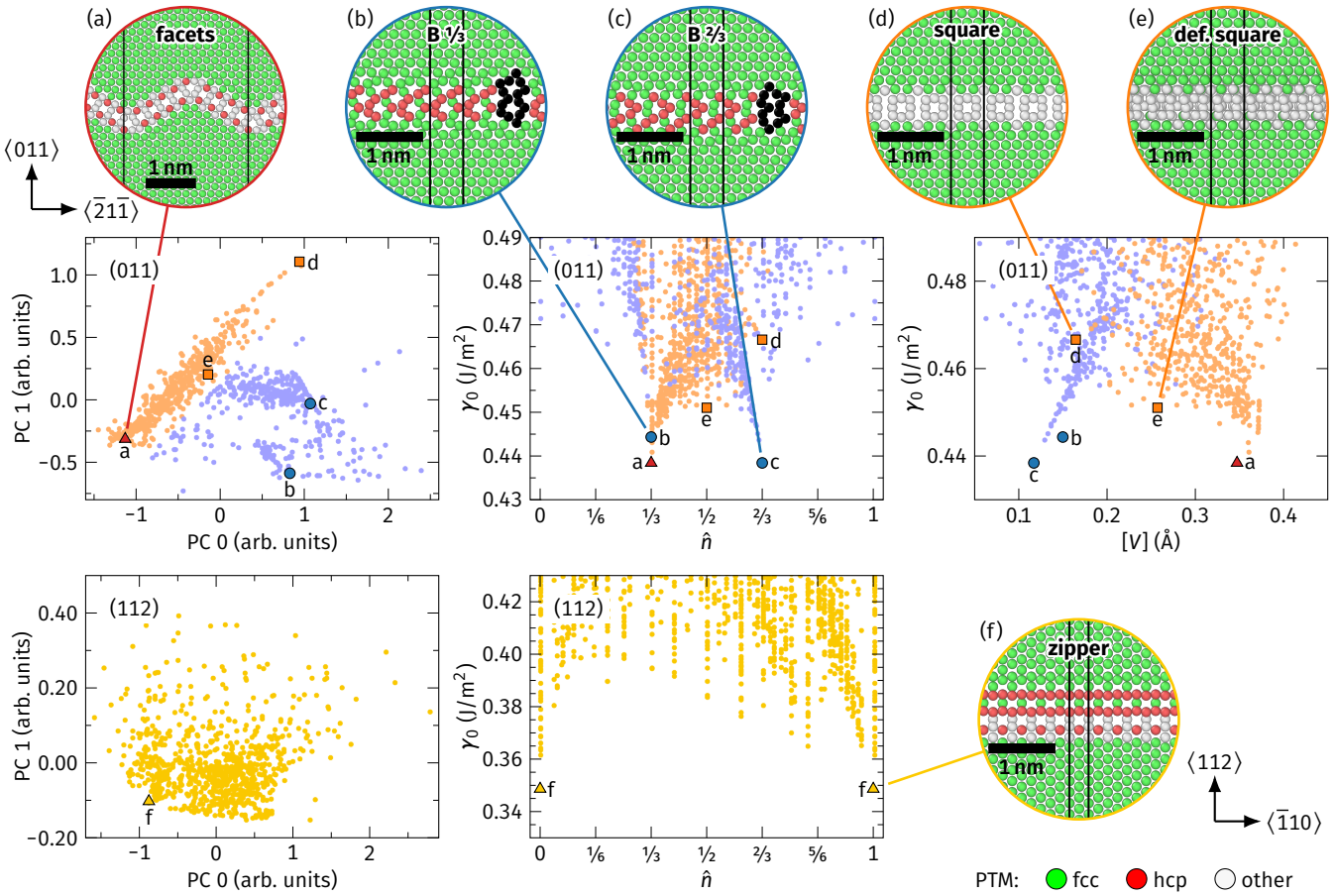


FIG. 2. Results of the GB structure search. The graphs in the top row show excess properties obtained for the (011) GB plane, the bottom row shows excess properties for the (112) GB plane. For (011), the structures shown in subfigures (a)–(e) are representatives of low-energy GB phases. They are also indicated in the graphs. Using PCA, we plot the first two principal components PC 0 and PC 1. At least two groups, containing the square and faceted structures (orange), as well as the B structures (blue) can be distinguished. For (112) GB planes, only the zipper structure (f) and defective variants were found. Additional analysis and data is provided in Supplemental Figs. S1 and S2. We show that all low-energy, faceted structures that we obtained are made of zipper facets in Supplemental Fig. S3.

Σ37c GB [30, 34]. On the (112) GB plane, we found only the zipper structure [31, 33, 35, 36]. This zipper structure is also present in the faceted structures on the (011) GB plane. While the structure of the short facets in Fig. 2(a) looks visually distinct from the zipper structure in Fig. 2(f), a detailed analysis (Supplemental Fig. S3) shows that all faceted (011) boundaries always consist of zipper structures, although they might be elastically distorted.

Both B ⅓ and B ⅔ are very similar in terms of structure, GB energy, excess volume, and excess stresses. They are thus most likely microstates of the same GB phase. The square motifs without defects have a relatively high GB energy, which is why we also show the lowest-energy, defective square-like motif at $\hat{n} = 0.5$. We conclude that three GB phases can occur in Σ3 $[11\bar{1}]$ (011) tilt GBs in Al: B, square, and faceted zipper. In a previous work on $[11\bar{1}]$ tilt GBs with misorientation angles $\theta < 60°$, it was found that the zipper facets are nanofaceted, occurring as a domino GB phase [15], while for $\theta = 60°$ (Σ3) the facets grow. In Cu, domino/pearl phase transitions were observed [30, 32]. This leads us to the hypothesis that the faceting/defaceting transition in Σ3 GBs is analogous to the domino/pearl transition, except for the length of the facets.

## V. FACETING TRANSITION AS A GRAIN BOUNDARY PHASE TRANSITION

### A. Prediction for infinitely long facets

The thermodynamic (meta-)stability [64] of GB phases can be described by their excess free energy $\gamma$, which we calculated using the QHA [51, 52]. To compare the GB energy of faceted GBs to non-faceted GBs, it needs to be renormalized: the GB area is $1/\cos\phi$ times larger in a GB faceted into segments inclined by $\phi$ towards the average

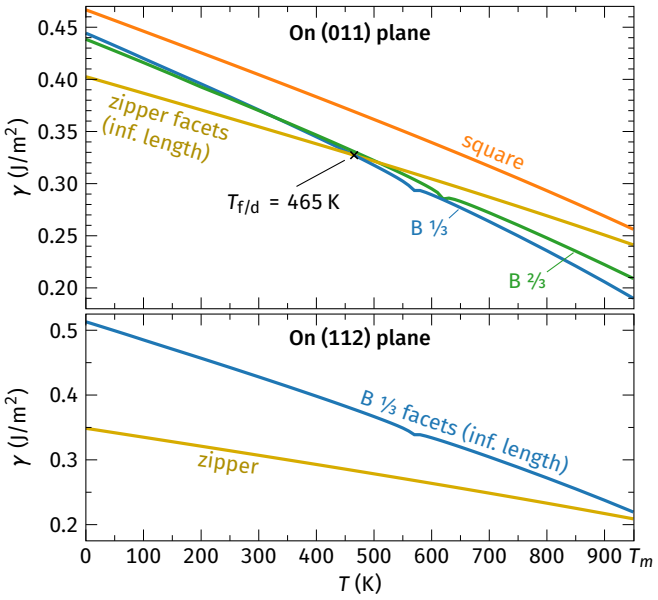


FIG. 3. GB excess free energy as a function of temperature for the discovered GB phases. For the (011) plane, the temperature $T_{\mathrm{f/d}}$ for the transition between zipper facets and a flat B phase is marked. The excess free energy of a faceted B phase on the (112) plane is so high that zipper stays stable up to the melting point $T_m$. For the B structures, there is a small dip in the data around 600 K. This is an unphysical numerical issue with the potential, most likely a bond length being stretched beyond the potential's cutoff radius due to thermal expansion. Here, classical free energies are presented, which are the relevant values for classical MD simulations. Supplemental Fig. S4 shows that the inclusion of quantum-mechanical effects only significantly affects the excess free energy below around 100 K.

GB plane. Additionally, the junctions between facets each contribute a defect energy $E_{\mathrm{core}}/t$, where $t$ is the length of the junction (here along the tilt axis direction). Due to the GB excess stress and potentially due to the dislocation character of the facet junction, elastic interactions have to be included, too [8]. This results in [8, 15]

$$\gamma = \frac{\gamma_{\mathrm{facet}}(T)}{\cos\phi} + \frac{E_{\mathrm{core}}}{tL} + K\frac{\ln(L/\delta_0)}{L}, \qquad (10)$$

where $L$ is the facet length and the last term represents the elastic interactions with $K$ being a constant and $\delta_0$ being the effective core size of the junction. For simplicity, we will assume that the junction energies are independent of temperature. For infinite facet lengths, only the first term remains nonzero, which is also the lowest possible GB energy of a faceted $\Sigma3$ $[11\bar{1}]$ tilt GB [15].

Figure 3 shows the results of QHA calculations for infinite facet lengths. A GB with a (011) plane would thus facet into zipper segments at low temperatures and defacet at high temperatures by transitioning into the B phase. A GB with a (112) plane, however, would favor the zipper structure up to the melting point. This is because the zipper phase is generally a low-energy GB phase, which is only made unfavorable on the (011) plane by the increased GB area due to faceting. The square phase does not play a role, due to its high energy.

### B. Transformation kinetics

In reality, when facets nucleate from a flat boundary, they need to grow from short to long facet lengths. We therefore constructed {112}-faceted GBs on the average (011) plane with varying lengths and $\hat{n} = 0$ as described in Ref. [15]. We also performed GRIP structure searches with larger supercells to find faceted GBs with $\hat{n} \neq 0$. Figure 4(a) shows the GB energies as a function of facet length $L$. Equation 10 fits well to the data (lines in the graph). The structures with $\hat{n} \neq 0$ differ by the type of their facet junction, but have the same facet structure (Supplemental Fig. S3), leading to large GB energy differences at short facet lengths. This difference becomes negligible at large facet lengths. We also estimated the change of the faceting/defaceting transition temperature

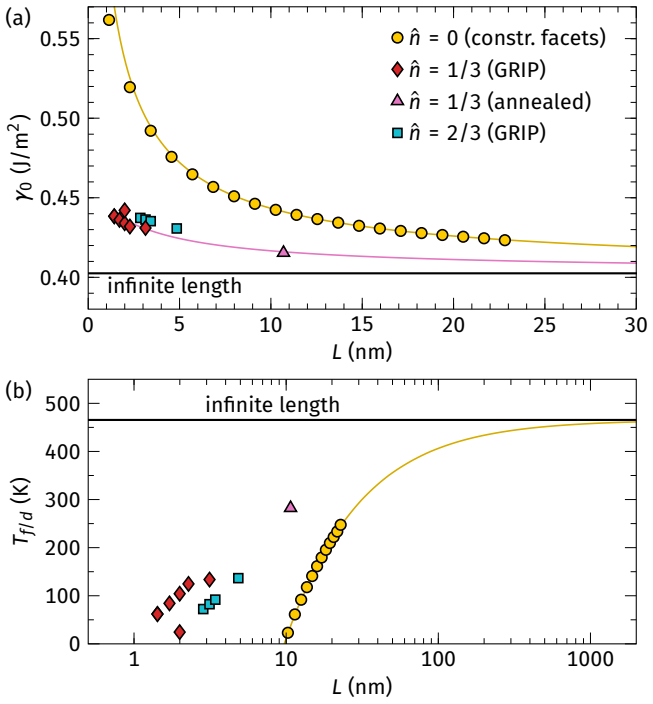


FIG. 4. Influence of the finite length of {112} facets located on an average (011) GB plane. (a) Ground state energy $\gamma_0$ of faceted zipper GBs as a function of facet length $L$. Differences in energy, especially at small $L$, are the result of different facet junction energies as a function of $\hat{n}$. The lines represent a fit of Eq. 10 to the data. Data points for $\hat{n} = 0$ were constructed by joining zipper facets as described in Ref. [15]. For $\hat{n} = 1/3$ and 2/3 the structures were obtained with GRIP. We replicated one sample with $\hat{n} = 1/3$ along the $y$ direction and annealed it to obtain longer facet lengths. (b) By adding the facet junction energies to the excess free energies from Fig. 3(a), we can estimate the change of the transition temperature $T_{\mathrm{f/d}}$ for different facet lengths.

$T_{\mathrm{f/d}}$ in Fig. 4(b), if the facet length were constrained (e.g., due to a finite size simulation cell). Transversely, this can be interpreted as a critical nucleus size as a function of temperature.

Additionally, the zipper facets themselves exhibit values of $\hat{n} = 0$, while $\hat{n} = 1/3$ or $2/3$ for the different B structures. Consequently, the growth of faceted structures from the B phase—or vice versa—requires either diffusion or leaves behind defects in the GB. As such, we cannot take the theoretical value of $T_{\mathrm{f/d}}$ as a given and the actual kinetics in a real sample will depend on the local point defect concentrations in and near the GB.

We nevertheless verified our results using various MD simulations. For this, we constructed bicrystals with an average (011) GB plane, a given $\hat{n}$ value, and a random GB structure and annealed them at $T = 400$, 500, 600, and 700 K for 30 ns.

For $\hat{n} = 0$, we started with a periodic simulation cell with a size in $y$ direction that admits a maximum facet length of approximately 9 nm [Fig. 5(a)]. Our previous results predict that a faceted GB with those facet lengths could never be stable [Fig. 4(b)] and the MD simulations support this: from 400 to 700 K, we obtain flat GBs with defective B structures. Larger simulations show sharply faceted boundaries up to 500 K and flat boundaries at 700 K, with a mix in between [Fig. 5(b)–(c)]. The faceted GBs contain zipper structures, the flat ones defective B structures (circular insets). These results can be reproduced both by starting from an already faceted GB and from a flat GB. The transition temperature significantly exceeds the prediction by the QHA (Fig. 3), but by inspecting Fig. 2, we can see that GRIP only found high-energy GBs at $\hat{n} = 0$, meaning that the B phase is much less stable there. A transition between $\hat{n}$ values would require open surfaces [39] and much longer MD simulation timescales than feasible for these system sizes.

For $\hat{n} = 1/3$ [Fig. 5(d)–(e)], the facet junction energy is lower, and smaller facets can occur. We found a transition temperature between 500 and 575 K. This is still higher than predicted by the QHA. However, the B structures are not pristine, but the GBs are very rough. It appears that this finite-temperature effect, which was not considered in the GRIP structure search, raises the free energy of the B structures and thereby the transition temperature. The free energy differences of the GBs are also quite small and any numerical errors can lead to quite large deviations in predicted transition temperature. Qualitatively, the MD simulations support our theory, especially since we find clear zipper structures in the faceted GBs and (defective) B structures in the flat GBs (see circular insets in Fig. 5).

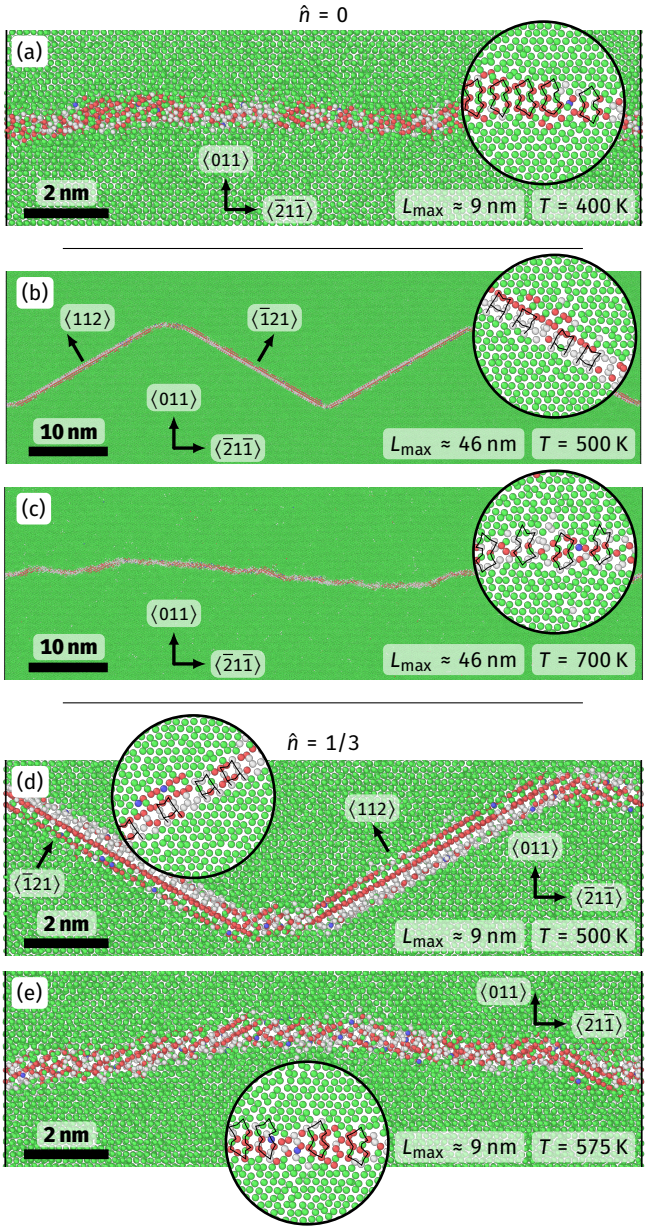


FIG. 5. Snapshots from MD simulations of $\Sigma 3$ $[11\bar{1}]$ (011) GBs. (a) A GB with $\hat{n} = 0$ does not exhibit any faceting. Here, the simulation cell size admits a maximum facet length of $L_{\max} = 9$ nm and therefore the facet junction energy is too high (see also Fig 4). (b)–(c) When allowing facet lengths up to 46 nm, a transition can be observed. (d)–(e) For $\hat{n} = 1/3$, the facet junction energies are lower. We observe faceting up to 500 K (d), while a rough but flat GB occurs at 575 K and above (e). In between, we observe a mix. The round insets show a zoom onto a slice with a thickness of 3 atomic layers, which allows to indentify the atomic motifs of the GB. We find zipper structures in the faceted GBs and B structures in the flat GBs. Indicated crystal directions refer to the lower crystallite. Equivalent crystal directions according to the misorientation in the upper crystallite not shown.

## VI. DISCUSSION IN THE CONTEXT OF PRIOR OBSERVATIONS REPORTED IN THE LITERATURE

The original observation [6] placed the faceting/defaceting transition at roughly 500 K, which fits well with the free energy prediction and MD simulations given the expected uncertainty of the transition temperature as discussed before. The good agreement obtained with the Zha09 potential is due to the accurate reproduction of the experimental melting point and of the GB energies (see Appendix A). Prior MD simulations have qualitatively similar results as the original experiments and our results, but did not investigate the transition as a GB phase transition [9]. We also found that the potentials used in previous simulation studies are flawed (see Appendix A). Here, we therefore shed light on the faceting/defaceting transition as a non-congruent GB phase transition.

In contrast, a study on epitaxial growth of Al films on alumina did not reveal any defaceting upon annealing, but instead simply reported the evolution of a maze structure of $\Sigma3$ $[11\bar{1}]$ {112} GBs [65]. Figure 3(b) explains this: GBs on {112} planes have no driving force to facet at all. The zipper GB phase, which is native to this plane, has such low energy that it will not transition into anything else. Consequently, any {112} GB would be stable. The present study only considers the case of a bicrystal with an average {011} GB plane. In a real polycrystal the transition to {112} facets might not be reversible if the microstructure reaches a deep energy minimum for its GB network. This is consistent with the equilibrium shape of a polyhedral grain in an infinite matrix: The interface stiffness tensor of Ni $\Sigma3$ $[11\bar{1}]$ boundaries shows that {112} facets are stable compared to {011} facets [66]. The same considerations apply for Al—given the lower GB energy of {112} facets compared to {011} facets—at least at low temperatures.

On the theory side, some previous models explain the faceting/defacting transition as a faceting refinement (or roughening) transition, where the configurational entropy of small facets overcomes their energy cost at the critical temperature [67, 68]. At low temperatures the facets are long and clearly defined, at high temperatures the facets are small and fluctuate. Direct atomistic simulations of this phenomenon were not provided. Here, we instead clearly observe the structural change between zipper facets and the B phase in MD simulations.

## VII. CONCLUSION

Experiments showed that $\Sigma3$ $[11\bar{1}]$ (011) tilt GBs in Al are sharply faceted at lower temperatures, while becoming flat above 500 K [6]. This phenomenon was investigated and modeled in the intervening years [9, 16, 67, 68], but the exact nature of the transition remained unclear. Here, we use atomistic computer simulations to show that this faceting/defaceting transition is in fact a non-congruent, first order GB phase transition. At low temperatures, the facets consist of the low-energy zipper GB phase. At high temperatures, the flat B phase becomes stable and the facets disappear. The faceting and defaceting are therefore controlled by the thermodynamic stability of their different atomic-scale structures.

We can relate this transition of the $\Sigma3$ GB ($\theta = 60°$) to the congruent GB phase transitions in related boundaries with lower misorientation angles ($\theta < 60°$): The B phase of the present work also appears as a motif in the pearl GB phase of the $\Sigma37c$ boundary [32]. The zipper facets are energetically driven to shrink to nanoscale size for $\theta < 60°$ and form the domino phase. That congruent pearl-to-domino transition becomes a non-congruent faceting/defacting transition for the $\Sigma3$ GB.

## VIII. DATA AVAILABILITY

The data that support the findings of this article are openly available [75].

## IX. ACKNOWLEDGMENTS

The authors thank Saba Saood for providing insights into her experimental work on Al GBs. This work was supported by the National Research Foundation of Korea (NRF) funded by the Korea government (Ministry of Science and ICT) (No. RS-2023-00254343). T.B. acknowledges funding from the European Research Council (ERC) under the European Union's Horizon 2020 research and innovation program (Grant agreement No. 787446; GB-CORRELATE).

Y.C. conducted the bulk of the simulations, while T.B. was responsible for some supplemental simulations. Y.C. and T.B. analyzed the data and wrote the initial manuscript draft. T.B. conceptualized and supervised the project.

### Appendix A: Evaluation of empirical potentials

We considered a range of classical empirical potentials from the literature and the NIST Interatomic Potentials Repository [42] for our simulations. We used several EAM potentials, designated as Vot86 [76], Jac87 [77], Mis99 [78], Stu00 [79], Zop03 [80], Liu04 [81], Zho04 [82], Men08 [83], Win09 [84], and Zha09 [41], as well as an MEAM potential, Pas15 [85]. We reconstructed the Vot86 potential based on the data in the original publications (the notebook and resulting potential file is available in the supporting data [75]). The Mis99 potential is the modified version described in Refs. [34, 86], which should give the same results as the original potential, apart from reducing numerical noise especially in the second derivatives required for phonon calculations. The parametrization for

TABLE I. Material properties of Al computed with the (M)EAM potentials compared to literature values (ref.). The reference values for the experimental ground-state energies $E_0^{\mathrm{fcc}}$ are from Ref. [69], while the experimental lattice constant $a_0^{\mathrm{fcc}}$, elastic constants $c_{ij}$, and the melting point $T_m$ are from Ref. [70]. The energy difference $E_{\mathrm{fcc}\to\mathrm{hcp}}$ between hcp and fcc crystal structures was calculated in the present work using DFT (we used primitive unit cells and a $21 \times 21 \times 21$ $k$-point grid, but otherwise the same parameters as described in Sec. III C). The vacancy formation energy $E_{f,\mathrm{vac}}$ is also an experimental value [71]. The surface energy $\gamma_{(111)}$ is from DFT simulations [72]. We used the literature review in Ref. [73] to collect data for values of the experimental stacking-fault energy $\gamma_{\mathrm{SF}}$ and DFT values for the unstable stacking-fault energy $\gamma_{\mathrm{USF}}$. The maximum shear stress $\tau_{\mathrm{SF}}$ along the generalized stacking-fault curve is from DFT calculations [74].

| | $E_0^{\mathrm{fcc}}$ (eV/atom) | $a_0^{\mathrm{fcc}}$ (Å) | $E_{\mathrm{fcc}\to\mathrm{hcp}}$ (eV/atom) | $c_{11}$ (GPa) | $c_{12}$ (GPa) | $c_{44}$ (GPa) | $T_m$ (K) | $E_{f,\mathrm{vac}}$ (eV) | $\gamma_{(111)}$ (J/m$^2$) | $\gamma_{\mathrm{SF}}$ (mJ/m$^2$) | $\gamma_{\mathrm{USF}}$ (mJ/m$^2$) | $\tau_{\mathrm{SF}}$ (GPa) |
|---|---|---|---|---|---|---|---|---|---|---|---|---|
| ref. | −3.39 | 4.050 | 0.03 | 107 | 60 | 28 | 933 | 0.67 | 1.199 | 135–200 | 175–224 | 2.8 |
| Zha09 | −3.361 | 4.032 | 0.003 | 105 | 70 | 44 | 951 | 0.74 | 0.733 | 15.9 | 107.2 | 1.9 |
| Vot86 | −3.360 | 4.050 | 0.014 | 107 | 65 | 32 | 602 | 0.63 | 0.820 | 75.5 | 93.1 | 1.5 |
| Jac87 | −3.388 | 3.988 | −0.001 | 111 | 85 | 46 | – | 1.16 | 0.908 | −6.0 | 88.1 | 1.8 |
| Mis99 | −3.360 | 4.050 | 0.028 | 114 | 62 | 32 | 1042 | 0.68 | 0.870 | 145.5 | 167.3 | 2.3 |
| Stu00 | −3.390 | 4.050 | 0.005 | 95 | 68 | 42 | 933 | 0.89 | 0.618 | 21.3 | 99.2 | 1.8 |
| Zop03 | −3.360 | 4.050 | 0.022 | 117 | 60 | 32 | 871 | 0.71 | 0.601 | 113.8 | 149.7 | 2.3 |
| Liu04 | −3.360 | 4.032 | 0.024 | 119 | 63 | 33 | 884 | 0.68 | 0.912 | 129.5 | 163.4 | 2.3 |
| Zho04 | −3.580 | 4.050 | 0.001 | 105 | 60 | 28 | 577 | 0.67 | 0.909 | – | – | – |
| Men08 | −3.411 | 4.045 | 0.028 | 105 | 59 | 31 | 926 | 0.66 | 0.428 | 127.1 | 219.7 | 3.7 |
| Win09 | −2.646 | 4.025 | 0.030 | 114 | 62 | 31 | 846 | 0.66 | 0.876 | 140.9 | 178.9 | 2.6 |
| Pas15 | −3.360 | 4.050 | 0.040 | 114 | 62 | 45 | 944 | 0.67 | 0.718 | 186.5 | 305.0 | 4.4 |

Jac87 was extracted from Ref. [87], which is part of the OpenKIM project [88, 89]. All other potentials were obtained from the NIST Interatomic Potentials Repository [42].

We then proceeded to evaluate the accuracy of these potentials against reference data from experiment or DFT. Bulk properties for fcc Al and the cohesive energy for hcp Al have been calculated as described in Ref. [34] and the results are listed in Table I. Cohesive energies, lattice constants, and elastic constants are reasonable for all potentials, except for Jac87 in which hcp is the stable phase and except for Win09 whose cohesive energy is too low. We therefore did not consider Jac87 in further simulations. The energy difference between fcc and hcp is often underestimated, as discussed below in more detail in the context of the stacking-fault energy. The $c_{44}$ elastic constant is often slightly overestimated. Melting point calculations were taken from Ref. [90] where available, otherwise they were computed with the software from that publication. Vot86 and Zho04 significantly underestimate the melting point, while the closest matches are Stu00, Men08, Zha09, and Pas15. Vacancy formation energies are once again in a reasonable range for all potentials, except Jac87. The (111) surface energies are underestimated by all potentials, which is a known issue with EAM-type potentials. When calculating the stacking-fault energies, the Zho04 potential yielded different results when constructing the stacking fault compared to producing it by gradual displacement of two halves of a perfect crystal. The latter is performed to obtain the unstable stacking-fault energy via a generalized stacking-fault energy curve [91–94]. Both methods must yield the same result, which points to numerical issues with the Zho04 potential, where slightly different defect configurations have significantly different energies. We therefore also excluded the Zho04 potential from further consideration. The Mis99, Liu04, Men08, and Win09 potentials yield (unstable) stacking-fault energies within the ranges reported in the literature. These potentials should therefore be preferred when simulating plasticity. Our potential of choice—Zha09—is poorly reproducing the stacking-fault energies. As outlined below, it is however an excellent match for the GB excess properties required in this paper.

We also require a reasonable description of free energies as a function of temperature. Figure 6 shows the linear thermal expansion coefficients compared with literature values. The combination of thermal expansion coefficient and melting point is a good indicator of the quality of the free energy as a function of temperature and the values are reliably accessible experimentally. In order to include quantum effects into the otherwise classical MD simulations, we used a quantum thermal bath (QTB) [98, 99] instead of the typical classical thermostats. We then fitted a Grüneisen equation of state [97, 100] to the data and show it in Fig. 6 alongside literature data [95–97]. Note that the QTB approach is approximate [99, 101, 102], but we ensured that the results coincide with the thermal expansion with classical thermostats at high temperatures (see Supplemental Fig. S5). Furthermore, we also calculated the thermal expansion using the QHA with PHONOPY [103, 104]. We found, however, that the QHA approach is unreliable with most potentials; only Zha09 coincides at all temperatures (see inset of Fig. 6 and Supplemental Fig. S5 for a more detailed discussion). We conclude that only Zha09 has both reasonable values for thermal expansion and melting point, as well as reliable QHA results across the temperature range.

We next move on to discuss the suitability of the po-

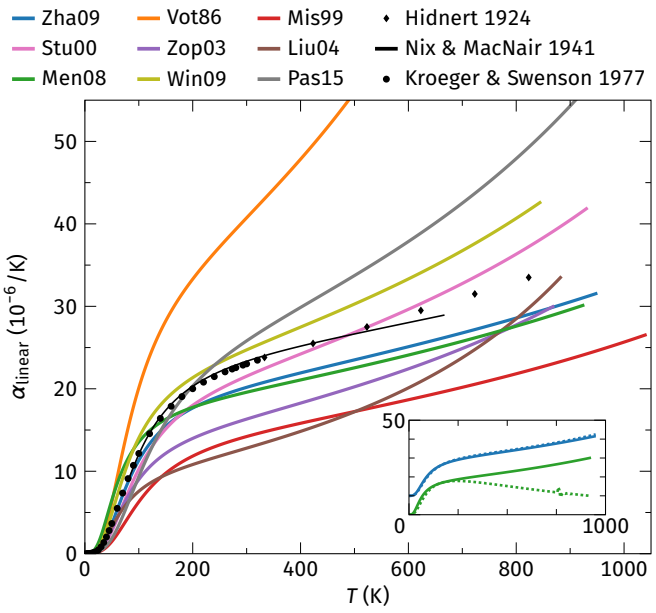


FIG. 6. Linear thermal expansion coefficients. Black points are experimental data from Hidnert [95], as well as Kroeger and Swenson [96]. The black line is a fit to the Grüneisen equation of state from Nix and MacNair [97]. Results for the empirical potentials were obtained by equilibrating with a QTB at 50 K temperature intervals and subsequently fitting the Grüneisen equation of state to the data. The plots end at the melting point. The inset shows a comparison of this method to thermal expansion computed with the QHA for Zha09 and Men08 (dotted lines). Due to numerical problems with other potentials, only Zha09 has a match between methods (see also Supplemental Fig. S5).

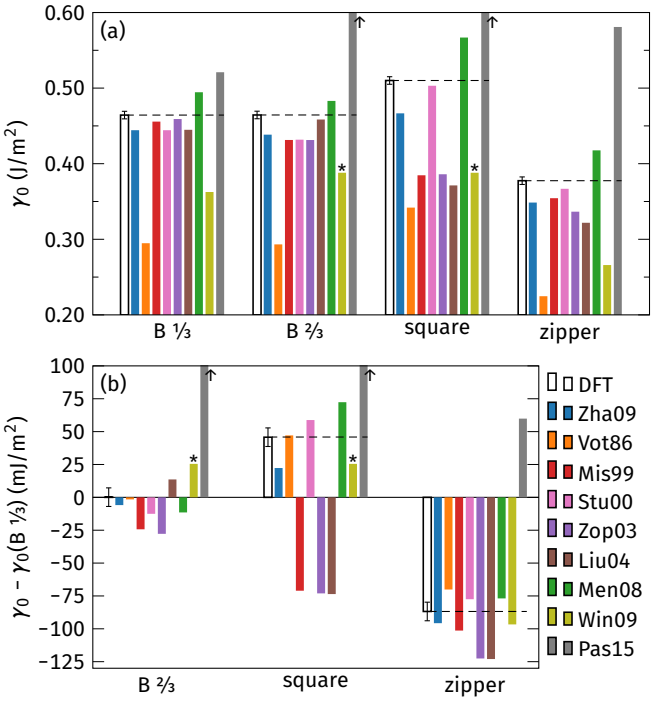


FIG. 7. (a) Comparison between GB energies calculated with DFT and with empirical potentials. The DFT error bars are conservatively estimated to be $\pm 5\,\mathrm{mJ/m^2} = \pm 0.3\,\mathrm{meV/Å^2}$ from variations in the GB energy with system size during convergence studies (Supplemental Figs. S7–S9). The B ⅔ structure minimized with the Win09 potential (marked by an asterisk) transforms into the square structure. (b) GB energy difference compared to B ⅓.

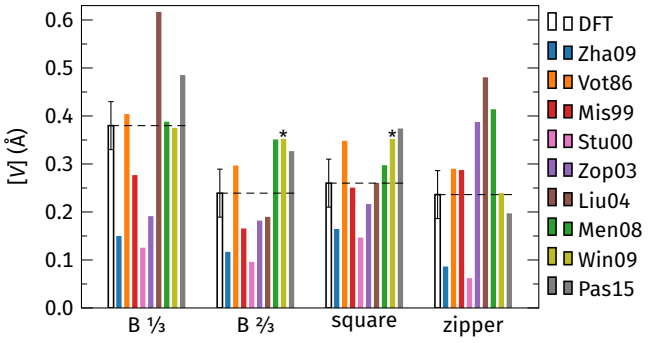


FIG. 8. Comparison between excess volumes calculated with DFT and with empirical potentials. The DFT error bars are conservatively estimated to be $\pm 0.05\,Å$ from variations in the GB energy with system size during convergence studies (Supplemental Figs. S7–S9). The B ⅔ structure minimized with the Win09 potential (marked by an asterisk) transforms into the square structure.

tentials for simulating GBs. For this, we first used DFT calculations to establish the excess GB properties for the B ⅓, B ⅔, square, and zipper GB phases. We used the calculations from Ref. [36] for zipper, and calculated the missing values here (Supplemental Figs. S6–S9). We obtained the GB energy $\gamma_0$ and compare it with the results obtained using the interatomic potentials in Fig. 7. We find that the Mis99, Zop03, and Liu04 potentials predict that the square GB phase is more stable than the B phase, which is contradicted by DFT. Furthermore, when using the Win09 potential, the B ⅔ structure becomes unstable and transforms into the square structure. The GB energies using the Pas15 potential are generally too high and the zipper phase's energy is much too high compared to the B ⅓ structure. We therefore exclude these potentials from further consideration for our GBs, as they would not be able to accurately predict the GB phase transition. Additionally, we ran GRIP structure searches for all potentials (Supplemental Fig. S10). The results confirm the calculations performed on the B ⅓, B ⅔, square, and zipper structures.

Out of the remaining potentials, the Vot86 and Men08 potentials reproduce the excess volume better than the Zha09 and Stu00 potentials (Fig. 8). We believe this to be less important than accurate energies and thermal expansion for our present investigation and therefore do not dismiss the Zha09 and Stu00 potentials here.

Instead, we investigated the GBs under different applied stresses $\sigma_{33}$. The change of excess potential energy

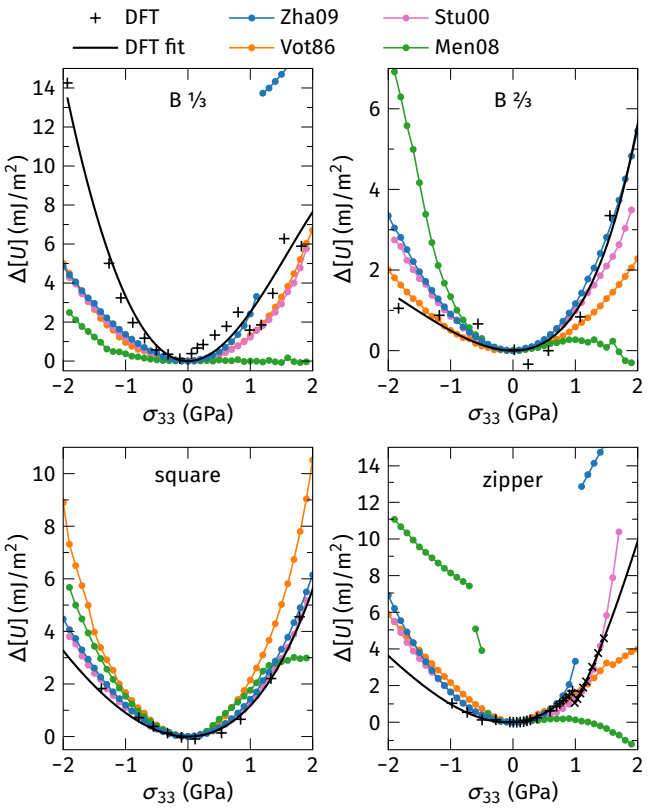


FIG. 9. Change of excess energy with applied stress $\sigma_{33}$. For DFT, the data points represent individual calculations and the lines are polynomial fits to the data.

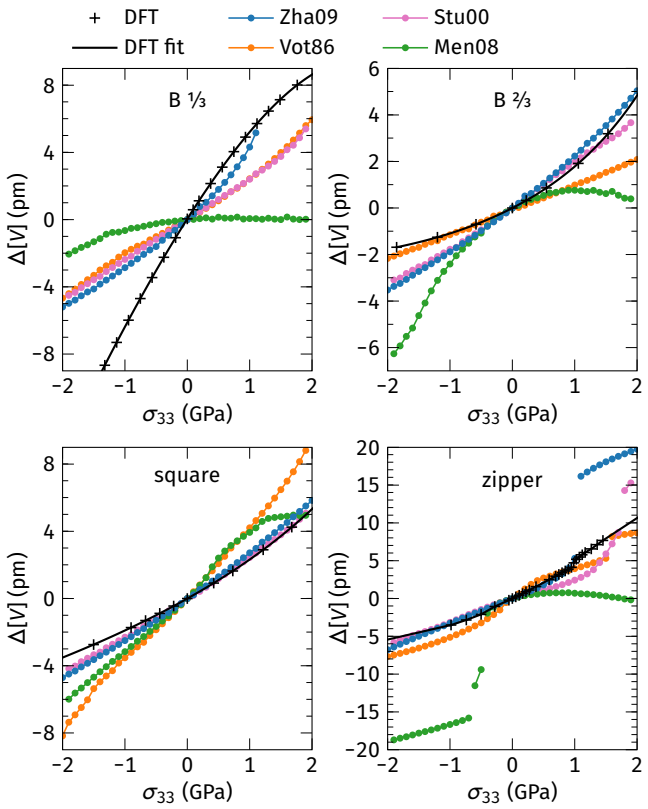


FIG. 10. Change of excess volume with applied stress $\sigma_{33}$. For DFT, the data points represent individual calculations and the lines are polynomial fits to the data.

with stress is presented in Fig. 9. None of the potentials perfectly match the GB's stiffness calculated with DFT. However, the Zha09 potential is a close match under tension, although it can be too soft or too stiff under compression. The Stu00 potential is of comparable quality and the Vot86 potential is qualitatively correct, but matches the DFT curves less well. The Men08 potential seems to exhibit softening/instability under tension. For the zipper phase, a transition between microstates under stress or strain has been observed before [36] and manifests here as a discontinuity in the energy curve. Such a transition between microstates is simply a sudden, but slight rearrangement of a GB atom in a shallow double-well potential. The Zha09 potential reproduces this transition at 1 GPa accurately, although the change in energy is much too high. The Vot86 and Stu00 potential predict this transition at the wrong stress and the Men08 potential even exhibits the transition under compression instead of tension. A similar microstate transition occurs with the Zha09 potential in the B ⅓ structure, but DFT calculations are inconclusive: some scatter is observed in the data, but no clear trends could be found. All of these findings are qualitatively matching to the evolution of excess volume under stress (Fig. 10).

Finally, numerical issues can occur when derivatives of the potential energy are required, such as in the case of QHA, where the force constant matrix contains the second derivatives of the potential energy. This is because numerical derivates amplify any noise or discontinuities present in the interatomic potential. We tested all potentials by starting once from an fcc unit cell and once from a B ⅓ GB and then straining the simulation box (Fig. 11 and Supplemental Figs. S11 and S12). We used fine-grained scaling factors, recorded the potential energy at each step (without additional relaxation of the atomic positions for computational efficiency), and calculated the derivatives using the finite difference method. Of the potentials under consideration, only the Zha09 potential is smooth, which is the expected result. The Vot86 potential exhibits some noise at a specific strain, which is most likely related to atoms leaving the cutoff radius. The Stu00 potential contains slight numerical noise, as well as a discontinuity in the second derivative. The Men08 potential is somewhat more noisy. Supplemental Figs. S11 and S12 contain data for all potentials and also explain some of the previously observed shortcomings of potentials we excluded from consideration.

In summary, we chose the Zha09 potential for its accurate reproduction of GB energies and thermal expansion coefficients. It is also smooth and the thermal expansion computed using QHA coincides with the QTB method and matches well to the experiments. We would recom-

mend this potential for GB (free) energy calculations and GB structure search as performed in the present paper. The main shortcoming we observed is the underestimation of the stacking-fault energy, which makes Zha09 unsuitable for simulations of plasticity. For MD simulations of plasiticity that also include GBs, we would recommend the Men08 potential, even though it has some numerical issues.

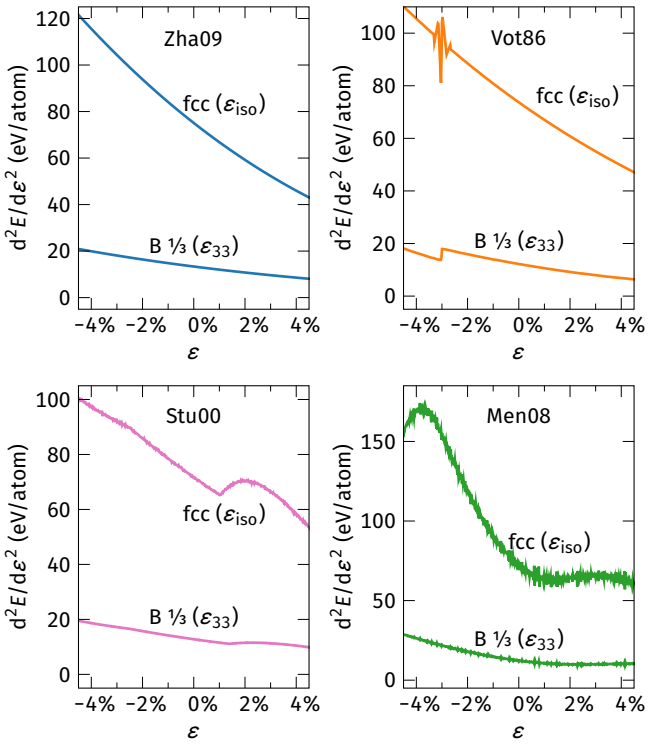


FIG. 11. Second derivative of the potential energy with strain, computed using finite differences. For each potential, both an fcc unit cell and a B ⅓ GB were strained; fcc hydrostatically and the GB along the $z$ direction. These plots reveal numerical problems with cutoffs, noise, and fluctuating curvature of the empirical potentials.


[1] G. Gottstein, *Physical Foundations of Materials Science*, 1st ed. (Springer, Berlin, Germany, 2004).

[2] P. Lejček, *Grain Boundary Segregation in Metals* (Springer, Berlin, Germany, 2010).

[3] L. Priester, *Grain Boundaries: From Theory to Engineering* (Springer, Berlin, Germany, 2013).

[4] W. R. Wagner, T. Y. Tan, and R. W. Balluffi, Faceting of high-angle grain boundaries in the coincidence lattice, Philos. Mag. **29**, 895 (1974).

[5] A. Brokman, P. D. Bristowe, and R. W. Balluffi, Atomistic faceting of asymetric tilt boundaries, Scr. Metall. **15**, 201 (1981).

[6] T. E. Hsieh and R. W. Balluffi, Observations of roughening/de-faceting phase transitions in grain boundaries, Acta Metall. **37**, 2133 (1989).

[7] B. B. Straumal, S. A. Polyakov, E. Bischoff, W. Gust, and E. J. Mittemeijer, Faceting of Σ3 and Σ9 grain boundaries in copper, Interface Sci. **9**, 287 (2001).

[8] J. C. Hamilton, D. J. Siegel, I. Daruka, and F. Léonard, Why do grain boundaries exhibit finite facet lengths?, Phys. Rev. Lett. **90**, 246102 (2003).

[9] Z. X. Wu, Y. W. Zhang, and D. J. Srolovitz, Grain boundary finite length faceting, Acta Mater. **57**, 4278 (2009).

[10] A. D. Banadaki and S. Patala, A simple faceting model for the interfacial and cleavage energies of Σ3 grain boundaries in the complete boundary plane orientation space, Comput. Mater. Sci. **112**, 147 (2016).

[11] G. P. Dimitrakopulos, T. H. Karakostas, and R. C. Pond, The defect character of interface junction lines, Interface Sci. **4**, 129 (1997).

[12] R. C. Pond and V. Vítek, Periodic grain boundary structures in aluminium I. A combined experimental and theoretical investigation of coincidence grain boundary structure in aluminium, Proc. R. Soc. Lond. A **357**, 453 (1997).

[13] D. L. Medlin, K. Hattar, J. A. Zimmerman, F. Abdeljawad, and S. M. Foiles, Defect character at grain boundary facet junctions: Analysis of an asymmetric $\Sigma = 5$ grain boundary in Fe, Acta Mater. **124**, 383 (2017).

[14] R. Hadian, B. Grabowski, M. W. Finnis, and J. Neugebauer, Migration mechanisms of a faceted grain boundary, Phys. Rev. Mater. **2**, 043601 (2018).

[15] T. Brink, L. Langenohl, S. Pemma, C. H. Liebscher, and G. Dehm, Stable nanofacets in [111] tilt grain boundaries of face-centered cubic metals, Phys. Rev. Mater. **8**, 063606 (2024).

[16] B. B. Straumal, O. A. Kogtenkova, A. S. Gornakova, V. G. Sursaeva, and B. Baretzky, Review: grain boundary faceting-roughening phenomena, J. Mater. Sci. **51**, 382 (2016).

[17] T. Frolov and Y. Mishin, Phases, phase equilibria, and

phase rules in low-dimensional systems, J. Chem. Phys. **143**, 044706 (2015).
[18] M. Tang, W. C. Carter, and R. M. Cannon, Diffuse interface model for structural transitions of grain boundaries, Phys. Rev. B **73**, 024102 (2006).
[19] S. J. Dillon, M. Tang, W. C. Carter, and M. P. Harmer, Complexion: A new concept for kinetic engineering in materials science, Acta Mater. **55**, 6208 (2007).
[20] P. R. Cantwell, M. Tang, S. J. Dillon, J. Luo, G. S. Rohrer, and M. P. Harmer, Grain boundary complexions, Acta Mater. **62**, 1 (2014).
[21] P. R. Cantwell, T. Frolov, T. J. Rupert, A. R. Krause, C. J. Marvel, G. S. Rohrer, J. M. Rickman, and M. P. Harmer, Grain boundary complexion transitions, Annu. Rev. Mater. Res. **50**, 465 (2020).
[22] W. D. Kaplan, D. Chatain, P. Wynblatt, and W. C. Carter, A review of wetting versus adsorption, complexions, and related phenomena: the Rosetta Stone of wetting, J. Mater. Sci. **48**, 5681 (2013).
[23] J. W. Gibbs, *The Collected Works of J. Willard Gibbs, Volume 1: Thermodynamics* (Yale University Press, New Haven, CT, USA, 1948).
[24] E. W. Hart, Two-dimensional phase transformation in grain boundaries, Scr. Metall. **2**, 179 (1968).
[25] E. W. Hart, Grain boundary phase transformations, in *The Nature and Behavior of Grain Boundaries*, edited by H. Hu (Plenum Press, New York, USA, 1972) pp. 155–170.
[26] W. Cahn, J., Transitions and phase equilibria among grain boundary structures, J. Phys. Colloques **43**, C6 (1982).
[27] C. Rottman, Theory of phase transitions at internal interfaces, J. Phys. Colloques **49**, C5 (1988).
[28] T. Frolov and Y. Mishin, Thermodynamics of coherent interfaces under mechanical stresses. I. Theory, Phys. Rev. B **85**, 224106 (2012).
[29] T. Frolov and Y. Mishin, Thermodynamics of coherent interfaces under mechanical stresses. II. Application to atomistic simulation of grain boundaries, Phys. Rev. B **85**, 224107 (2012).
[30] T. Meiners, T. Frolov, R. E. Rudd, G. Dehm, and C. H. Liebscher, Observations of grain-boundary phase transformations in an elemental metal, Nature **579**, 375 (2020).
[31] T. Meiners, J. M. Duarte, G. Richter, G. Dehm, and C. H. Liebscher, Tantalum and zirconium induced structural transitions at complex [111] tilt grain boundaries in copper, Acta Mater. **190**, 93 (2020).
[32] L. Langenohl, T. Brink, R. Freitas, T. Frolov, G. Dehm, and C. H. Liebscher, Dual phase patterning during a congruent grain boundary phase transition in elemental copper, Nat. Commun. **13**, 3331 (2022).
[33] L. Langenohl, T. Brink, G. Richter, G. Dehm, and C. H. Liebscher, Atomic-resolution observations of silver segregation in a [111] tilt grain boundary in copper, Phys. Rev. B **107**, 134112 (2023).
[34] T. Brink, L. Langenohl, H. Bishara, and G. Dehm, Universality of grain boundary phases in fcc metals: Case study on high-angle [111] symmetric tilt grain boundaries, Phys. Rev. B **107**, 054103 (2023).
[35] S. Saood, T. Brink, C. H. Liebscher, and G. Dehm, Influence of variation in grain boundary parameters on the evolution of atomic structure and properties of [111] tilt boundaries in aluminum, Acta Mater. **268**, 119732 (2024).
[36] S. Saood, T. Brink, C. H. Liebscher, and G. Dehm, Microstates and defects of incoherent Σ3 [111] twin boundaries in aluminum, Acta Mater. **243**, 118499 (2023).
[37] A. Morawiec, On 'interface-plane scheme' and symmetric grain boundaries, Z. Kristallogr. **227**, 199 (2012).
[38] J. W. Cahn, Thermodynamics of solid and fluid surfaces, in *Interfacial Segregation*, edited by W. C. Johnson and J. M. Blakely (American Society of Metals, Metals Park, OH, USA, 1979) pp. 379–399.
[39] T. Frolov, D. L. Olmsted, M. Asta, and Y. Mishin, Structural phase transformations in metallic grain boundaries, Nat. Commun. **4**, 1899 (2013).
[40] J. Hickman and Y. Mishin, Extra variable in grain boundary description, Phys. Rev. Mater. **1**, 010601 (2017).
[41] V. V. Zhakhovskii, N. A. Inogamov, Y. V. Petrov, S. I. Ashitkov, and K. Nishihara, Molecular dynamics simulation of femtosecond ablation and spallation with different interatomic potentials, Appl. Surf. Sci. **255**, 9592 (2009).
[42] NIST Interatomic Potentials Repository, National Institute of Standards and Technology, https://www.ctcms.nist.gov/potentials, https://doi.org/10.18434/m37.
[43] A. P. Thompson, H. M. Aktulga, R. Berger, D. S. Bolintineanu, W. M. Brown, P. S. Crozier, P. J. in 't Veld, A. Kohlmeyer, S. G. Moore, T. D. Nguyen, R. Shan, M. J. Stevens, J. Tranchida, C. Trott, and S. J. Plimpton, LAMMPS - a flexible simulation tool for particle-based materials modeling at the atomic, meso, and continuum scales, Comput. Phys. Commun. **271**, 108171 (2022), https://lammps.org/.
[44] S. Plimpton, Fast parallel algorithms for short-range molecular dynamics, J. Comp. Phys. **117**, 1 (1995), https://lammps.org/.
[45] G. Kresse and J. Hafner, Ab initio molecular dynamics for liquid metals, Phys. Rev. B **47**, 558 (1993).
[46] G. Kresse and J. Hafner, Ab initio molecular-dynamics simulation of the liquid-metal–amorphous-semiconductor transition in germanium, Phys. Rev. B **49**, 14251 (1994).
[47] G. Kresse and J. Furthmüller, Efficiency of ab-initio total energy calculations for metals and semiconductors using a plane-wave basis set, Comput. Mater. Sci. **6**, 15 (1996).
[48] G. Kresse and J. Furthmüller, Efficient iterative schemes for ab initio total-energy calculations using a plane-wave basis set, Phys. Rev. B **54**, 11169 (1996).
[49] J. Janssen, S. Surendralal, Y. Lysogorskiy, M. Todorova, T. Hickel, R. Drautz, and J. Neugebauer, pyiron: An integrated development environment for computational materials science, Comput. Mater. Sci. **163**, 24 (2019).
[50] E. Chen, T. W. Heo, B. C. Wood, M. Asta, and T. Frolov, Grand canonically optimized grain boundary phases in hexagonal close-packed titanium, Nat. Commun. **15**, 7049 (2024).
[51] S. M. Foiles, Evaluation of harmonic methods for calculating the free energy of defects in solids, Phys. Rev. B **49**, 14930 (1994).
[52] R. Freitas, R. E. Rudd, M. Asta, and T. Frolov, Free energy of grain boundary phases: Atomistic calculations for Σ5(310)[001] grain boundary in Cu, Phys. Rev. Mater. **2**, 093603 (2018).
[53] P. M. Larsen, S. Schmidt, and J. Schiøtz, Robust structural identification via polyhedral template matching, Modell. Simul. Mater. Sci. Eng. **24**, 055007 (2016).
[54] A. Stukowski, Visualization and analysis of atomistic

simulation data with OVITO – the Open Visualization Tool, Modell. Simul. Mater. Sci. Eng. **18**, 015012 (2010), https://ovito.org/.
[55] See Supplemental Material at [link to be inserted by publisher] for supplemental data and analyses.
[56] S. Saood, T. Brink, C. H. Liebscher, and G. Dehm, Datasets for the paper "microstates and defects of incoherent Σ3 [111] twin boundaries in aluminum", Zenodo (2022).
[57] P. E. Blöchl, Projector augmented-wave method, Phys. Rev. B **50**, 17953 (1994).
[58] J. P. Perdew, K. Burke, and M. Ernzerhof, Generalized gradient approximation made simple, Phys. Rev. Lett. **77**, 3865 (1996).
[59] G. Kresse and D. Joubert, From ultrasoft pseudopotentials to the projector augmented-wave method, Phys. Rev. B **59**, 1758 (1999).
[60] H. J. Monkhorst and J. D. Pack, Special points for Brillouin-zone integrations, Phys. Rev. B **13**, 5188 (1976).
[61] K. Pearson, LIII. On lines and planes of closest fit to systems of points in space, Philos. Mag. **2**, 559 (1901).
[62] H. Hotelling, Analysis of a complex of statistical variables into principal components, J. Educ. Psychol. **24**, 417 (1933).
[63] H. Hotelling, Analysis of a complex of statistical variables into principal components, J. Educ. Psychol. **24**, 498 (1933).
[64] Note that GBs are never thermodynamically stable. A system in thermodynamic equilibrium would only contain point defects. However, if we take the presence of a GB as a given, we can still formulate the relative stability of different GB phases using standard thermodynamics.
[65] G. Dehm, B. J. Inkson, and T. Wagner, Growth and microstructural stability of epitaxial Al films on (0001) $\alpha$-$Al_2O_3$ substrates, Acta Mater. **50**, 5021 (2002).
[66] F. Abdeljawad, S. M. Foiles, A. Moore, A. R. Hinkle, C. Barr, N. M. Heckman, K. Hattar, and B. L. Boyce, The role of the interface stiffness tensor on grain boundary dynamics, Acta Mater. **158**, 440 (2018).
[67] I. Daruka and J. C. Hamilton, Atomistic and lattice model of a grain boundary defaceting phase transition, Phys. Rev. Lett. **92**, 246105 (2004).
[68] C. Qiu, M. Salvalaglio, D. J. Srolovitz, and J. Han, Interface faceting-defaceting mediated by disconnections, Acta Mater. **251**, 118880 (2023).
[69] C. Kittel, *Introduction to Solid State Physics*, 8th ed. (Wiley, Hoboken, New Jersey, USA, 2005).
[70] J. Rumble, ed., *CRC Handbook of Chemistry and Physics*, 103rd ed. (CRC Press, Boca Raton, FL, USA, 2022).
[71] H. Ullmaier, ed., *Atomic Defects in Metals*, Landolt-Börnstein – Group III Condensed Matter, Vol. 25 (Springer, Berlin, Germany, 1991).
[72] L. Vitos, A. V. Ruban, H. L. Skriver, and J. Kollár, The surface energy of metals, Surf. Sci. **411**, 186 (1998).
[73] N. Bernstein and E. B. Tadmor, Tight-binding calculations of stacking energies and twinnability in fcc metals, Phys. Rev. B **69**, 094116 (2004).
[74] S. Ogata, J. Li, and S. Yip, Ideal pure shear strength of aluminum and copper, Science **298**, 807 (2002).
[75] Y. Choi and T. Brink, Datasets for "Faceting transition in aluminum as a grain boundary phase transition", Zenodo (2025), doi:10.5281/zenodo.15674815.
[76] A. F. Voter and S. P. Chen, Accurate interatomic potentials for Ni, Al and $Ni_3Al$, MRS Online Proceedings Library **82**, 175 (1986).
[77] K. W. Jacobsen, P. Stoltze, and J. K. Nørskov, A semi-empirical effective medium theory for metals and alloys, Surf. Sci. **366**, 394 (1996).
[78] Y. Mishin, D. Farkas, M. J. Mehl, and D. A. Papaconstantopoulos, Interatomic potentials for monoatomic metals from experimental data and ab initio calculations, Phys. Rev. B **59**, 3393 (1999).
[79] J. B. Sturgeon and B. B. Laird, Adjusting the melting point of a model system via Gibbs-Duhem integration: Application to a model of aluminum, Phys. Rev. B **62**, 14720 (2000).
[80] R. R. Zope and Y. Mishin, Interatomic potentials for atomistic simulations of the Ti-Al system, Phys. Rev. B **68**, 024102 (2003).
[81] X.-Y. Liu, F. Ercolessi, and J. B. Adams, Aluminium interatomic potential from density functional theory calculations with improved stacking fault energy, Modell. Simul. Mater. Sci. Eng. **12**, 665 (2004).
[82] X. W. Zhou, R. A. Johnson, and H. N. G. Wadley, Misfit-energy-increasing dislocations in vapor-deposited CoFe/NiFe multilayers, Phys. Rev. B **69**, 144113 (2004).
[83] M. I. Mendelev, M. J. Kramer, C. A. Becker, and M. Asta, Analysis of semi-empirical interatomic potentials appropriate for simulation of crystalline and liquid Al and Cu, Philos. Mag. **88**, 1723 (2008).
[84] J. M. Winey, A. Kubota, and Y. M. Gupta, A thermodynamic approach to determine accurate potentials for molecular dynamics simulations: thermoelastic response of aluminum, Modell. Simul. Mater. Sci. Eng. **17**, 055004 (2009).
[85] M. I. Pascuet and J. R. Fernández, Atomic interaction of the MEAM type for the study of intermetallics in the Al–U alloy, J. Nucl. Mater. **467**, 229 (2015).
[86] T. Brink, L. Langenohl, H. Bishara, and G. Dehm, Dataset for "Universality of grain boundary phases in fcc metals: Case study on high-angle [111] symmetric tilt grain boundaries", Zenodo (2022), doi:10.5281/zenodo.7358052.
[87] J. K. Nørskov, K. W. Jacobsen, and P. Stoltze, EMT potential for Al developed by Jacobsen, Stoltze, and Norskov (1996) v001, OpenKIM (2019).
[88] E. B. Tadmor, R. S. Elliott, J. P. Sethna, R. E. Miller, and C. A. Becker, The potential of atomistic simulations and the knowledgebase of interatomic models, JOM **63**, 17 (2011).
[89] R. S. Elliott and E. B. Tadmor, Knowledgebase of Interatomic Models (KIM) application programming interface (API), OpenKIM (2011).
[90] L.-F. Zhu, J. Janssen, S. Ishibashi, F. Körmann, B. Grabowski, and J. Neugebauer, A fully automated approach to calculate the melting temperature of elemental crystals, Comput. Mater. Sci. **187**, 110065 (2021).
[91] V. Vítek, Thermally activated motion of screw dislocations in B.C.C. metals, Phys. Status Solidi B **18**, 687 (1966).
[92] V. Vítek, Intrinsic stacking faults in body-centred cubic crystals, Philos. Mag. **18**, 773 (1968).
[93] J. A. Zimmerman, H. Gao, and F. F. Abraham, Generalized stacking fault energies for embedded atom FCC metals, Modell. Simul. Mater. Sci. Eng. **8**, 103 (2000).
[94] J. Cai, C. Lu, P. H. Yap, and Y. Y. Wang, How to affect stacking fault energy and structure by atom relaxation,

Appl. Phys. Lett. **81**, 3543 (2002).
[95] P. Hidnert, Thermal expansion of aluminum and various important aluminum alloys, Scientific Papers of the Bureau of Standards **19**, 697 (1924).
[96] F. R. Kroeger and C. A. Swenson, Absolute linear thermal-expansion measurements on copper and aluminum from 5 to 320 K, J. Appl. Phys. **48**, 853 (1977).
[97] F. C. Nix and D. MacNair, The thermal expansion of pure metals: Copper, gold, aluminum, nickel, and iron, Phys. Rev. **60**, 597 (1941).
[98] H. Dammak, Y. Chalopin, M. Laroche, M. Hayoun, and J.-J. Greffet, Quantum thermal bath for molecular dynamics simulation, Phys. Rev. Lett. **103**, 190601 (2009).
[99] J.-L. Barrat and D. Rodney, Portable implementation of a quantum thermal bath for molecular dynamics simulations, J. Stat. Phys. **144**, 679 (2011).
[100] E. Grüneisen, Zustand des festen Körpers, in *Thermische Eigenschaften der Stoffe*, Handbuch der Physik, Vol. 10, edited by C. Drucker, E. Grüneisen, P. Kohnstamm, F. Körber, K. Scheel, E. Schrödinger, F. Simon, J. D. Waals, and F. Henning (Springer, Berlin, Heidelberg, 1926) pp. 1–59.
[101] A. H. Barrozo and M. de Koning, Comment on "Quantum thermal bath for molecular dynamics simulation", Phys. Rev. Lett. **107**, 198901 (2011).
[102] H. Dammak, M. Hayoun, Y. Chalopin, and J.-J. Greffet, Dammak et al. Reply, Phys. Rev. Lett. **107**, 198902 (2011).
[103] A. Togo, First-principles phonon calculations with phonopy and phono3py, J. Phys. Soc. Jpn. **92**, 012001 (2023).
[104] A. Togo, L. Chaput, T. Tadano, and I. Tanaka, Implementation strategies in phonopy and phono3py, J. Phys.: Condens. Matter **35**, 353001 (2023).